

Unusual Oxygen Partial Pressure Dependence of Electrical Transport of Single-Crystalline Metal Oxide Nanowires Grown by the Vapor–Liquid–Solid Process

Hiroshi Anzai,[†] Tsunaki Takahashi,^{*,‡,§} Masaru Suzuki,[‡] Masaki Kanai,[‡] Guozhu Zhang,[‡] Takuro Hosomi,^{‡,§} Takehito Seki,[§] Kazuki Nagashima,^{†,‡,§} Naoya Shibata,[§] and Takeshi Yanagida^{*,†,‡,§}

[†]Interdisciplinary Graduate School of Engineering Sciences, Kyushu University, 6-1 Kasuga-Koen, Kasuga, Fukuoka 816-8580, Japan

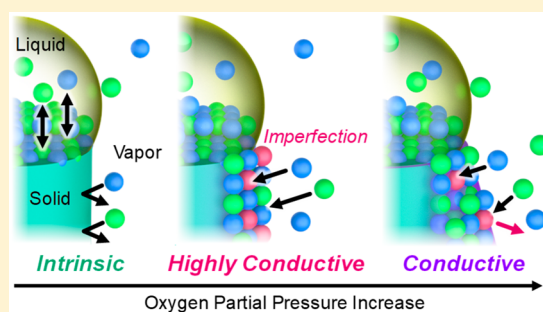
[‡]Institute for Materials Chemistry and Engineering, Kyushu University, 6-1 Kasuga-Koen, Kasuga, Fukuoka 816-8580, Japan

[§]Institute of Engineering Innovation, The University of Tokyo, 2-11-16 Yayoi, Bunkyo, Tokyo 113-8656, Japan

Supporting Information

ABSTRACT: In general, the electrical conductivities of *n*-type semiconducting metal oxide nanostructures increase with the decrease in the oxygen partial pressure during crystal growth owing to the increased number of crystal imperfections including oxygen vacancies. In this paper, we report an unusual oxygen partial pressure dependence of the electrical conductivity of single-crystalline SnO₂ nanowires grown by a vapor–liquid–solid (VLS) process. The electrical conductivity of a single SnO₂ nanowire, measured using the four-probe method, substantially decreases by 2 orders of magnitude when the oxygen partial pressure for the crystal growth is reduced from 10^{−3} to 10^{−4} Pa. This contradicts the conventional trend of *n*-type SnO₂ semiconductors. Spatially resolved single-nanowire electrical transport measurements, microstructure analysis, plane-view electron energy-loss spectroscopy, and molecular dynamics simulations reveal that the observed unusual oxygen partial pressure dependence of the electrical transport is attributed to the intrinsic differences between the two crystal growth interfaces (LS and VS interfaces) in the critical nucleation of the crystal growth and impurity incorporation probability as a function of the oxygen partial pressure. The impurity incorporation probability at the LS interface is always lower than that at the VS interface, even under reduced oxygen partial pressures.

KEYWORDS: Metal oxide nanowire, vapor–liquid–solid growth, oxygen partial pressure, unintentional carrier doping, crystal growth interface



Single-crystalline semiconducting metal oxide nanowires, such as SnO₂, ZnO, and TiO₂ nanowires, are promising nanomaterials for electronics, photonics, energy conversion, and biotechnology applications utilizing their ionicity-induced unique physical properties, which are hardly attainable in conventional covalent semiconducting materials including Si and compound semiconductors.^{1–7} These metal oxide semiconductors including SnO₂ are mostly *n*-type even without an intentional carrier doping during the crystal growth.^{8–15} The control and understanding of the unintentional carrier doping during the crystal growth are long-standing scientific issues for their semiconductor applications.^{16–20} For these *n*-type metal oxides, it is well-known that the oxygen partial pressure during the crystal growth strongly affects the electrical conductivity. In general, the electrical conductivities of *n*-type metal oxides increase with the decrease in the oxygen partial pressure during the crystal growth owing to the increased content of crystal imperfections including oxygen vacancies.^{21,22} The oxygen partial pressure dependences of the electrical conductivities of *n*-type metal oxides have been commonly observed for various

nanostructures, including thin films and nanoparticles grown by a vapor transport method, highlighting the universality.^{23–27}

This study demonstrates an unusual oxygen partial pressure P_{O_2} dependence of the electrical conductivity of single-crystalline SnO₂ nanowires grown by a vapor–liquid–solid (VLS) process, which is one of the popular vapor transport nanowire growth methods.^{5,28–30} The electrical conductivity of a single SnO₂ nanowire, measured by the four-probe method, substantially decreased by 2 orders of magnitude when P_{O_2} for the crystal growth was reduced from 10^{−3} to 10^{−4} Pa. This trend is completely different from the conventional trend of *n*-type SnO₂. Plane-view scanning transmission electron microscopy (STEM), electron energy-loss spectroscopy (EELS), and molecular dynamics (MD) simulations reveal that the observed unusual oxygen partial pressure dependence of the electrical

Received: November 19, 2018

Revised: March 2, 2019

Published: March 3, 2019

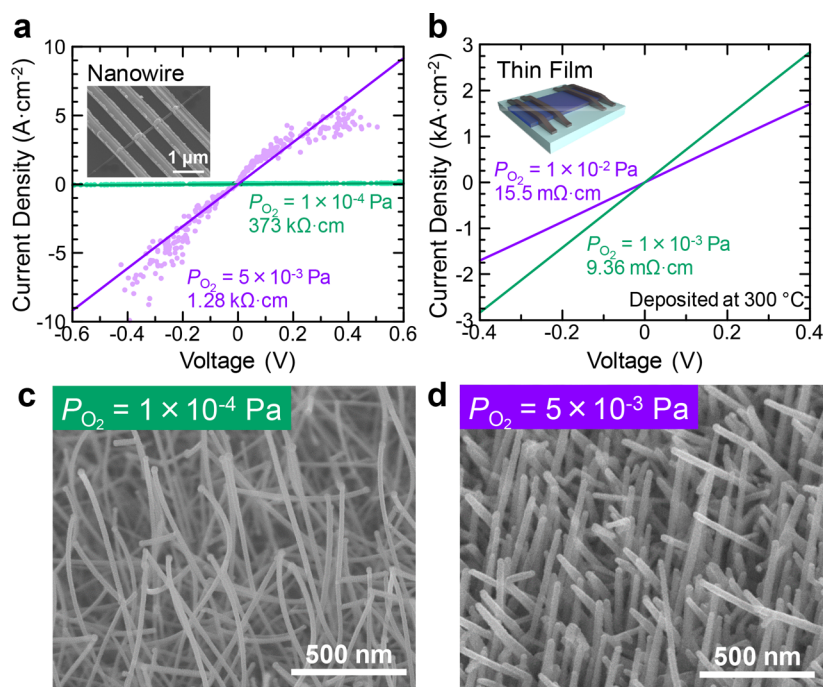


Figure 1. Current density–voltage characteristics of the (a) VLS-grown SnO_2 nanowires and (b) SnO_2 thin film deposited by PLD. SEM images of the SnO_2 nanowires obtained by the VLS processes at oxygen partial pressures (P_{O_2}) of (c) 1×10^{-4} and (d) 5×10^{-3} Pa. The other growth parameters including the Sn metal flux ($5.0 \times 10^{17} \text{ cm}^{-2} \text{ s}^{-1}$), temperature ($650 \text{ }^\circ\text{C}$), and Au catalyst thickness (0.7 nm) are common for these nanowires.

transport is attributed to the intrinsic differences between the two crystal growth interfaces (LS and VS interfaces) in the critical nucleation of the crystal growth and impurity incorporation probability upon the variation in the oxygen partial pressure.

Figure 1a shows typical current–voltage (I – V) characteristics of the SnO_2 nanowires grown at P_{O_2} of 1×10^{-4} and 5×10^{-3} Pa. The small P_{O_2} decrease leads to a significant increase in the nanowire resistivity over 2 orders of magnitude. In general, the resistivity of an n -type semiconducting metal oxide decreases under a reduced- P_{O_2} growth condition owing to the increased number of crystal imperfections including oxygen vacancies, which generate mobile electrons.^{23–27} It is worth noting that the observed P_{O_2} dependence of the VLS-grown SnO_2 nanowire resistivity is opposite to the general trend. As shown in Figure 1b, the conventional P_{O_2} dependence of the resistivity (higher P_{O_2} leads to a higher resistivity) was observed for SnO_2 thin films deposited under similar conditions to those of the nanowire growth. In addition to the electrical characteristics, the morphologies of the nanowires grown at the two different P_{O_2} values are different. Figures 1c,d show scanning electron microscopy (SEM) images of the SnO_2 nanowires grown at P_{O_2} of 1×10^{-4} and 5×10^{-3} Pa, respectively. The nontapered nanowires were grown at the lower P_{O_2} (1×10^{-4} Pa, Figure 1c), whereas the tapered nanowires were grown at the higher P_{O_2} (5×10^{-3} Pa, Figure 1d). The observed morphological difference seems to correlate to the P_{O_2} dependence of the VLS-grown SnO_2 nanowire resistivity.

In order to clarify the origin of the observed P_{O_2} effect on the electrical resistivity in Figure 1, we systematically investigate the morphologies and electrical properties of SnO_2 nanowires in a

wide range of P_{O_2} . Figure 2a shows the P_{O_2} dependence of the apparent nanowire resistivity, which is calculated using the nanowire diameter at the center between the two voltage electrodes in the four-probe measurement. In the low- P_{O_2} range (smaller than 1×10^{-3} Pa), the nanowires are almost electrically insulative, which indicates that the unintentional carrier doping is sufficiently suppressed in these nanowires. With the increase in P_{O_2} in the range of 1×10^{-3} to 5×10^{-3} Pa, the nanowire resistivity substantially decreases by 2 orders of magnitude, which corresponds to the trend in Figure 1a. With the further increase in P_{O_2} above 5×10^{-3} Pa, the nanowire resistivity begins to increase after reaching the minimum value. Therefore, two competing and contrary effects on the electrical resistivity are observed with the variation in P_{O_2} during the nanowire growth. First, the P_{O_2} dependence above 5×10^{-3} Pa, i.e., the increase in electrical resistivity with P_{O_2} , is consistent with those of conventional n -type semiconducting metal oxides based on the reduced number of crystal imperfections including oxygen vacancies at a higher P_{O_2} .^{23–27} Second, the contrary effect below 5×10^{-3} Pa must be originated from an event suppressing such crystal imperfections even under the reduced- P_{O_2} atmosphere. In the VLS nanowire growth process, two different crystal growth interfaces exist: LS and VS interfaces.^{31,32} We have recently reported that the two crystal growth interfaces have different impurity incorporation probabilities during the nanowire growth.³³ Therefore, the understanding of the P_{O_2} dependence of the crystal growth interface (i.e., the nanowire morphology) is important to explain the experimental trend below P_{O_2} of 5×10^{-3} Pa. Figure 2b shows the P_{O_2} dependences of the thin film growth rate and nanowire diameters at the tip (D_{tip}) and thickest (D_{max}) positions. The LS crystal growth occurs at the interface between the metal catalyst and nanowire,

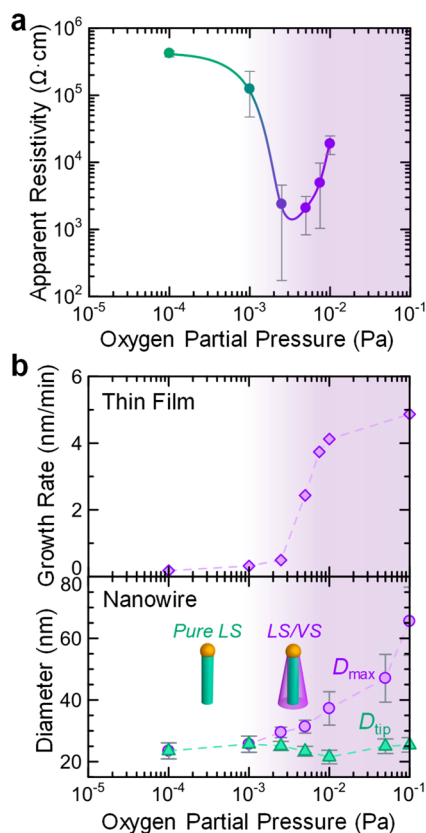


Figure 2. (a) P_{O_2} dependence of the apparent resistivity of the SnO_2 nanowires. The apparent resistivities are calculated using the nanowire diameters at the center between the two voltage electrodes of the four-terminal devices. The error bars are obtained as maximum/minimum values of three samples. An approximate curve is shown as a visual guide. (b) P_{O_2} dependences of the SnO_2 thin film growth rate (upper panel) and SnO_2 nanowire diameters at the tip (D_{tip}) and thickest position (D_{max}) for the 30 min growth (lower panel). The deposition conditions of the thin film are the same as those for the nanowires (lower graph) except for the Au catalyst deposition. The error bars of the nanowire data are obtained as the standard deviation of 50 samples.

whereas the VS crystal growth occurs on the nanowire sidewalls, yielding the tapered nanowire structures. Therefore, the difference between D_{tip} and D_{max} ($D_{\text{max}} - D_{\text{tip}}$) corresponds to the amount of crystal growth at the VS interface. As shown in Figure 2b, both D_{max} deviation from D_{tip} and nucleation for the thin film growth are initiated at the same P_{O_2} higher than 1×10^{-3} Pa. The good agreement between the tapered structure and thin film growth is a direct evidence that the crystal growth at the VS interface occurs at the higher P_{O_2} . The emergence of VS growth correlates with the substantial change in the nanowire resistivity around P_{O_2} of $1\text{--}5 \times 10^{-3}$ Pa in Figure 2a. The impurity incorporation probability at the LS interface is lower than that at the VS interface owing to the so-called annealing effect.³³ Therefore, the substantial change in the nanowire resistivity around P_{O_2} of $1\text{--}5 \times 10^{-3}$ Pa can be interpreted in terms of the competing effect between the VS and LS growth interfaces on the electrical resistivity (i.e., the degree of unintentional carrier doping).

The observed correlation between the emergence of the VS growth and higher electrical conduction can be directly validated by measuring position-dependent resistivities in a single tapered

nanowire, as the tapered nanowire should exhibit the spatial dependence of the electrical conductivity with the gradient of the VS growth along the axial direction. As shown in Figure 3a,b,

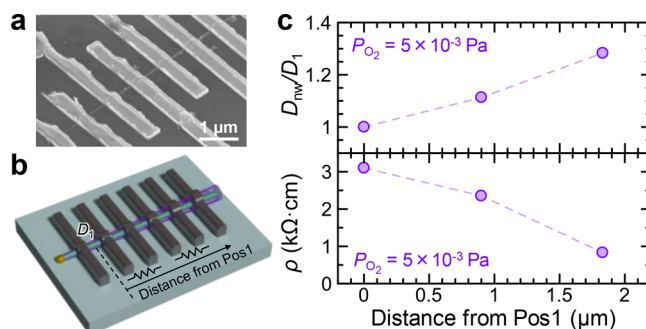


Figure 3. (a) SEM image and (b) schematic of the multiterminal single-nanowire device. (c) Positional dependences of the nanowire diameter and apparent resistivity. Upper graph: ratio of the nanowire diameter of each position (D_{nw}) and narrowest diameter between the electrodes (Pos1, D_1). Lower graph: apparent nanowire resistivity ρ .

we fabricated multiterminal single-nanowire devices. The device structure enables systematic electrical characterizations of the nanowire with the VS growth independent of the sample-to-sample variations in the nanowire diameters and/or amount of VS growth, which led to the error bars in Figure 2a. Figure 3c shows the position-dependent apparent resistivity and ratio of diameters (D_{nw}/D_1) for the tapered nanowire grown at P_{O_2} of 5×10^{-3} Pa, which has both LS and VS growth interfaces (LS/VVS nanowire). D_{nw} and D_1 are the nanowire diameters at each position and narrowest measured position, respectively. The diameter ratio D_{nw}/D_1 corresponds to the degree of nanowire tapering, i.e., the degree of crystal growth at the VS interface. The LS/VVS nanowire exhibits positional dependences of its structure and resistivity. The D_{nw}/D_1 increases, while the resistivity decreases from the nanowire tip to the base. The systematic correlation between the emergence of VS growth and electrical conductivity is a direct experimental evidence that the VS growth interface causes the unintentional carrier doping in the VLS-grown SnO_2 nanowires. Therefore, these results show that the unusual P_{O_2} dependence of the SnO_2 nanowire resistivity (the resistivity decreases with the increase in P_{O_2}) originates from the suppression of the unintentional carrier doping at the LS growth interface and unintentionally doped VS crystal growth interface at the higher- P_{O_2} range. It is worth noting that the diameter-dependent dopant incorporation/deactivation effect, which has been reported in intentionally doped Si VLS nanowires,^{34,35} possibly leads to the lower resistivities of the tapered or thicker nanowires in Figures 2 and 3. However, as shown in Supporting Information, the resistivity of the nontapered (pure LS) nanowires exhibits a weak dependence on the diameter. Furthermore, the unusual P_{O_2} dependence of the resistivity was also observed for nanowires having almost identical diameters of 36–38 nm (see Supporting Information). Therefore, the unusual P_{O_2} dependence cannot be explained by the diameter-dependent dopant effect.

Crystallographic and stoichiometric differences between the LS and VS crystal growth interfaces were directly analyzed by plane-view STEM and EELS. Parts a and b of Figure 4 show cross-sectional high-angle annular dark-field (HAADF) STEM

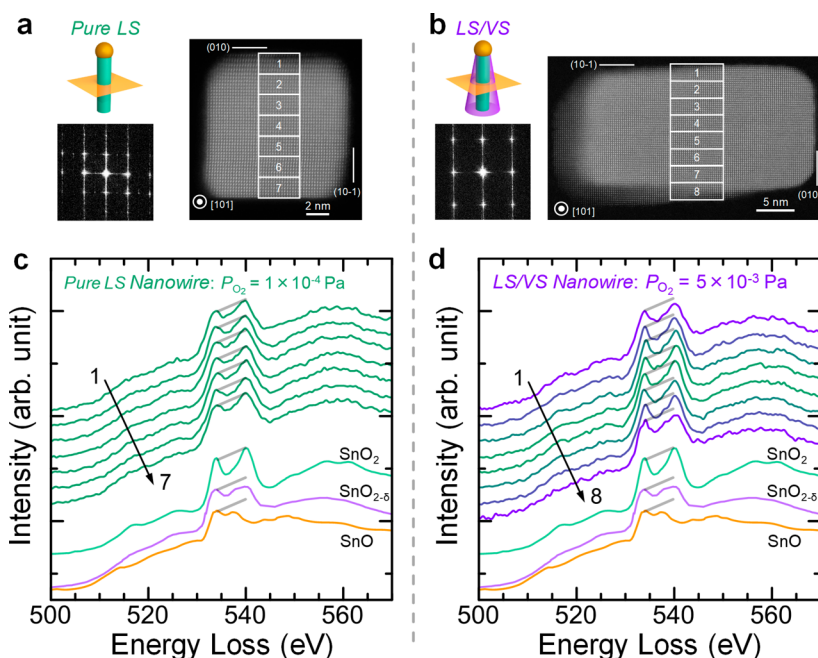


Figure 4. Cross-sectional HAADF STEM images of the (a) nontapered SnO_2 nanowire (grown at P_{O_2} of 1×10^{-4} Pa) and (b) tapered nanowire (grown at P_{O_2} of 5×10^{-3} Pa). EELS O–K-edge spectra of the numbered rectangular regions in the STEM images of the (c) nontapered and (d) tapered SnO_2 nanowires. The reference O–K-edge spectra of SnO_2 , $\text{SnO}_{2-\delta}$, and SnO are also shown.

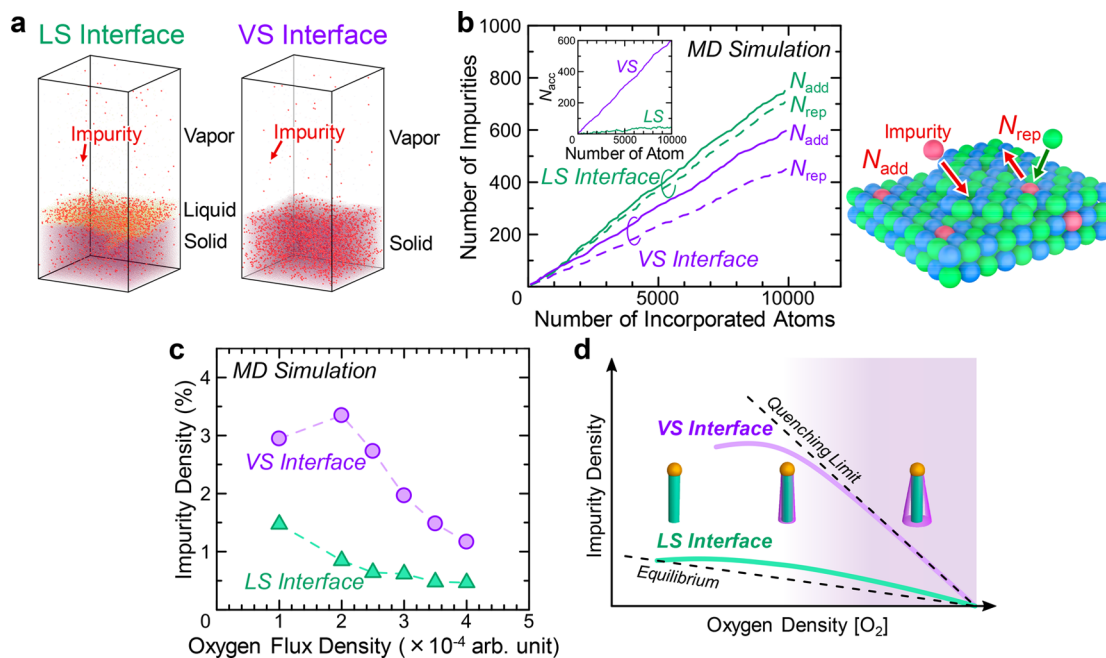


Figure 5. (a) Snapshots of the crystal growth MD simulations for both LS and VS interfaces in the presence of impurities under an oxygen flux density of 1×10^{-4} . Impurities are highlighted with larger diameters (red dots). (b) Numbers of added (N_{add}) and replaced (N_{rep}) impurity atoms against the number of total incorporated atoms during the LS and VS crystal growths under the oxygen flux density of 1×10^{-4} . The actual, or accumulated, number of impurity atoms N_{acc} , defined as $N_{\text{add}} - N_{\text{rep}}$, is shown in the inset. A schematic of the added and replaced impurity atoms during the LS and VS crystal growth is also shown. (c) Oxygen flux density dependences of the impurity densities for the LS and VS crystal growths. (d) Schematic of the impurity incorporation mechanisms of the LS and VS crystal growth interfaces.

images of the nontapered (pure LS, grown at P_{O_2} of 1×10^{-4} Pa) and tapered (LS/VS, grown at P_{O_2} of 5×10^{-3} Pa) SnO_2 nanowires, respectively. In the STEM images, the single-crystalline structures were observed for both nontapered and tapered nanowires, indicating that the crystal structures of the LS and VS crystal growth interfaces were consistent. A difference

in cross-sectional shape between the nontapered and tapered nanowires was also observed owing to the sidewall VS crystal growth of the tapered (LS/VS) nanowires. A spatially resolved EELS analysis was then performed for the pure LS and LS/VS nanowires. Parts c and d of Figure 4 show the spatial O–K-edge EELS spectra of the pure LS and LS/VS nanowires, respectively.

Reference O–K-edge spectra of SnO₂, SnO_{2-δ}, and SnO³⁶ are also shown for comparison. On the one hand, for the nontapered pure LS nanowire, the O–K-edge peak shapes are almost identical from the inner core to the outer regions and well agree with the reference SnO₂ spectrum, indicating that the LS interface crystal is stoichiometric SnO₂. On the other hand, for the tapered LS/V_S nanowire, the O–K-edge peaks show the spatial dependence; i.e., stoichiometric-SnO₂-like peak shapes in the inner core and oxygen-deficient-SnO_{2-δ}-like peak shapes in the outer regions are observed. As the outer regions of the tapered nanowire correspond to the V_S crystal growth on the nanowire sidewall, the spatial variation in the EELS spectra of the tapered nanowire is direct evidence that the unintentional doping (e.g., oxygen deficiencies) is triggered by the V_S crystal growth interface. Therefore, the origin of the unusual P_{O_2} dependence of the SnO₂ nanowire resistivity discussed above is supported by the observation of the stoichiometric SnO₂ growth at the LS interface and oxygen-deficient SnO_{2-δ} growth at the V_S interface.

Further microscopic insights into the P_{O_2} dependence of the electrical resistivity of the VLS-grown nanowires can be obtained by MD simulations. The MD simulation method is presented in detail in the [Methods](#) and [Supporting Information](#). In the MD simulations, impurity atoms are intentionally employed to model the dynamics of incorporation of crystal imperfections (e.g., oxygen vacancies) into the LS and V_S crystal growth interfaces. In the simulations, the relative interaction parameter of the impurities, ϵ' , is set to 0.7, where the incorporation of the impurity atoms into the solid phase destabilizes the solid structure. [Figure 5a](#) shows typical snapshots of the MD simulations during the LS and V_S crystal growths. [Figure 5b](#) shows the time-integrated numbers of impurity atoms added into the solid phase from the vapor or liquid phase, N_{add} , and time-integrated numbers of impurity atoms replaced with metal atoms or removed from the crystal, N_{rep} . These MD simulation results show that the crystal reconstruction during the LS crystal growth substantially suppresses the incorporation of impurities or oxygen vacancies into the LS growth interface, an effect similar to thermal annealing (see [Supporting Information](#)). To investigate the effects of the oxygen partial pressure on the impurity incorporation dynamics, the oxygen flux density (which corresponds to P_{O_2}) dependences of the impurity densities at both LS and V_S interfaces were calculated, as shown in [Figure 5c](#). In the whole oxygen flux range, the impurity density at the LS interface is lower than that at the V_S interface. The different oxygen flux dependences of the impurity densities for the LS and V_S interfaces can be theoretically interpreted in terms of equilibrium and quenching limit models, respectively, as illustrated in [Figure 5d](#). On the one hand, in the V_S crystal growth, the defect or impurity ratio α in the high-growth-rate range should converge to the quenching limit or limit of rapid solidification, where the ratio of atom species in the solid directly reflects the flux ratio. Therefore, the defect ratio is expressed as $\alpha = 1 - [O_2]/[Sn]$ in this limit, where $[O_2]$ and $[Sn]$ are the oxygen and Sn flux densities, respectively. On the other hand, in the LS crystal growth, where a high crystal reconstruction or annealing effect is observed owing to the affinity between liquid and metal/impurity atoms, the configuration of the solid remains near the equilibrium condition. In the equilibrium, the defect ratio can be approximated as $\alpha \approx (1 - [O_2]/[Sn]) \exp(-\Delta F/k_B T)$, where ΔF , k_B , and T are the free-energy

loss per site by replacing an oxygen atom with an impurity, Boltzmann constant, and temperature, respectively. The derivation of these equations is shown in the [Supporting Information](#). The calculated trends of the impurity densities for the LS and V_S growth interfaces shown in [Figure 5c](#) qualitatively agree with these two theoretically predicted curves, validating our MD simulations. The obtained relationships between the oxygen flux and impurity density for the two growth interfaces (LS and V_S) well explain the unique or unusual oxygen role in the electrical conductivity of the VLS-grown SnO₂ nanowires ([Figure 2a](#)). First, in the higher- P_{O_2} region where the V_S crystal growth is dominant ($>3 \times 10^{-3}$ Pa), the unintentional doping or impurities in the V_S crystal growth interface are suppressed with the increase in P_{O_2} , which is a widely known tendency in the *n*-type metal oxide thin film growth. Second, in the intermediate- P_{O_2} region where the V_S crystal growth starts ($1-3 \times 10^{-3}$ Pa), the total unintentional doping in the nanowires rapidly increases with P_{O_2} owing to the beginning of the V_S crystal growth with many impurities. Third, in the lower- P_{O_2} region where only the LS crystal growth occurs ($<1 \times 10^{-3}$ Pa), the annealing effect at the LS growth interface sufficiently suppresses the unintentional doping in the nanowires even at the oxygenless growth atmosphere. It is worth noting that the experimentally observed P_{O_2} effect on the LS and V_S growth interface nucleation ([Figure 2b](#)) is qualitatively supported by the MD simulations, as shown in [Supporting Information](#). The MD simulations show that the unique oxygen role in the electrical conduction of the VLS-grown SnO₂ nanowires originates from the strong impurity suppression at the near-equilibrium LS crystal growth interface and V_S crystal growth enhancement in the higher- P_{O_2} region.

In conclusion, we demonstrated the unusual oxygen partial pressure (P_{O_2}) dependence of the electrical conduction of the SnO₂ nanowires grown by the VLS process, opposite to the trend of conventional *n*-type semiconducting metal oxides. By precisely controlling P_{O_2} and evaluating the position-dependent electrical properties of a single nanowire, we showed that the unintentionally doped V_S crystal growth on the nanowire sidewall is the trigger of the unusual P_{O_2} dependence. The cross-sectional STEM and EELS analyses revealed that the oxygen-deficient SnO_{2-δ} growth at the V_S crystal interface is the origin of the unintentional doping in the V_S crystal. Through the numerical/theoretical investigation including the MD simulations, the mechanism of the unique oxygen role was attributed to the crystal reconstruction at the LS crystal growth interface, leading to the equilibrium condition. As intrinsic (without unintentional doping) oxide nanowires were successfully achieved on the basis of the present knowledge, our findings pave the way for a wide functionality of metal oxide nanostructures, which require intrinsic semiconductor properties as a base.

Methods. SnO₂ Nanowire Growth. The SnO₂ nanowires were grown on an Al₂O₃ (110) substrate (Electronics and Materials) by the pulsed-laser deposition (PLD) method through the VLS process.³⁷ A tablet of SnO₂ source (purity: 99.99%, Kojundo Chemical Laboratory) was utilized as the target for ablation by an ArF excimer laser ($\lambda = 193$ nm, Coherent, COMPex Pro). Prior to the nanowire growth, a thin film of Au (0.7 nm) was deposited onto the substrate by direct-current (DC) sputtering (SANYU Electron, SC-701HMC). The chamber for the crystal growth was initially evacuated below

5×10^{-5} Pa, and then an O₂/Ar mixture gas (purity: 99.9999%) was introduced with controlled oxygen partial pressure in the range of 10^{-4} – 10^{-1} Pa. The total pressure was maintained at 10 Pa in order to prevent Au catalyst consumption during the nanowire growth. The flux of vapor species was controlled by varying the energy density of the laser. Before the laser ablation, the substrate temperature was increased to 650 °C within 10 min, which was maintained during the nanowire growth. The growth time was 30–720 min. After the nanowire growth, the substrate was cooled to room temperature within 30 min. The Sn flux was quantitatively evaluated by a film deposition at room temperature in a 10 Pa O₂ atmosphere to avoid reevaporation from the substrate, which occurs under high-temperature conditions. The Sn flux was estimated using the density of SnO₂ and deposited-film thickness measured with a surface profiler (KLA Tencor, Alpha-Step IQ). The Sn flux was maintained at 5.0×10^{17} cm⁻² s⁻¹ for all nanowires. The morphology of the obtained SnO₂ nanowires was characterized by field-emission SEM (JEOL, JSM-7610F) at an accelerating voltage of 15 kV. The diameters and lengths of the nanowires were statistically evaluated based on 50 nanowires. We employed an STEM (JEOL, JEM-ARM300F) equipped with an EELS setup (GIF Quantum) at an accelerating voltage of 300 kV. For the STEM observations, the nanowires on the substrate were embedded in epoxy resin, mechanically polished, and then thinned by an ion beam. The probe size was approximately 0.06 nm. The EELS acquisition times for the LS and LS/VIS nanowires were 10 and 15 s, respectively, for each rectangle region. During the acquisitions, the probe scanned inside the rectangle regions. As the original reference spectra in Figure 4 are not calibrated, they were offset to align the first oxygen peak. The smoothed spectra were obtained by the weighted average method with a window of 1 eV.

Device Fabrication and Electrical Characterization. The devices for the electrical measurements were fabricated by electron beam (EB) lithography. The grown SnO₂ nanowires were dispersed in ethanol by sonication. The nanowires were then dropped onto a 100 nm thick SiO₂/n-type Si substrate with Ti (10 nm)/Pt (120 nm) pad electrodes patterned by EB lithography and radio frequency (RF) sputtering. EB lithography was then performed to obtain electrical contacts on the dropped nanowires. An EB resist (ZEON, ZEP520A-7) was coated by a spin coater (MIKASA, MS-A100), followed by EB exposure (Elionix) and development (ZEON, ZED-NS0). A 150 nm thick Pt was then deposited by RF sputtering (SEINAN) in a 0.3 Pa Ar atmosphere. Lift-off (*N,N*-dimethylformamide) and cleaning (acetone) processes were carried out to complete the device fabrication. The electrical measurements were performed using a semiconductor parameter analyzer (Keithley, 4200SCS) with a probe station at 10^{-2} Pa and room temperature. The resistances of the SnO₂ nanowires were measured using the four-probe technique to avoid overestimation owing to the contact resistance. The nanowire resistivity ρ was calculated assuming a circular cross section of the nanowire: $\rho = \pi R D_{\text{nw}}^2 / (4L)$, where R , D_{nw} , and L are the four-probe resistance, diameter of the nanowire, and length between the two voltage electrodes of each four-terminal device, respectively.

MD Simulation. The MD simulation was performed using a simple model of atom species of the metal oxide, impurities, and liquid catalyst. The characteristics of the solid growth and impurities incorporated into the solid for the VS and VLS systems were compared by independent calculations of the film-

like solid growths for both systems under equivalent conditions of the vapor flux. Further details of the simulation method are presented in the [Supporting Information](#).

■ ASSOCIATED CONTENT

Supporting Information

The Supporting Information is available free of charge on the ACS Publications website at DOI: [10.1021/acs.nanolett.8b04668](https://doi.org/10.1021/acs.nanolett.8b04668).

Oxygen partial pressure dependence of the SnO₂ thin film resistivity, growth rate and density of the SnO₂ nanowires, diameter dependence of the nanowire resistivity, MD simulation model, probability of impurity atom replacement at the LS/VIS crystal growth interface, simulated growth rate of the SnO₂ nanowires, equilibrium and quenching limit models for the crystal growth ([PDF](#))

■ AUTHOR INFORMATION

Corresponding Authors

*E-mail: takahashi.t@cm.kyushu-u.ac.jp.

*E-mail: yanagida@cm.kyushu-u.ac.jp.

ORCID

Tsunaki Takahashi: 0000-0002-2840-8038

Takuro Hosomi: 0000-0002-5649-6696

Kazuki Nagashima: 0000-0003-0180-816X

Naoya Shibata: 0000-0003-3548-5952

Takeshi Yanagida: 0000-0003-4837-5701

Notes

The authors declare no competing financial interest.

■ ACKNOWLEDGMENTS

This study was supported by KAKENHI (grant numbers: 17H04927, 18H01831, and 18H05243). T.Y. was supported by the ImPACT Program of the Council for Science, Technology, and Innovation (Cabinet Office, Government of Japan). T.T., T.H., K.N., and T.Y. were supported by JST CREST, Japan (grant number: JPMJCR1331). T.Y. and K.N. were supported by CAS-JSPS Joint Research Projects (Grant No. GJHZ1891). This study was performed under the Cooperative Research Program of “Network Joint Research Center for Materials and Devices” and MEXT Project of “Integrated Research Consortium on Chemical Sciences”.

■ REFERENCES

- (1) Keem, K.; Jeong, D.-Y.; Kim, S.; Lee, M.-S.; Yeo, I.-S.; Chung, U. I.; Moon, J.-T. *Nano Lett.* **2006**, *6*, 1454–1458.
- (2) Cheng, Y.; Xiong, P.; Yun, C. S.; Strouse, G. F.; Zheng, J. P.; Yang, R. S.; Wang, Z. L. *Nano Lett.* **2008**, *8*, 4179–4184.
- (3) Wang, X.; Zhou, J.; Song, J.; Liu, J.; Xu, N.; Wang, Z. L. *Nano Lett.* **2006**, *6*, 2768–2772.
- (4) Wang, Z. L.; Song, J. *Science* **2006**, *312*, 242–246.
- (5) Huang, M. H.; Mao, S.; Feick, H.; Yan, H.; Wu, Y.; Kind, H.; Weber, E.; Russo, R.; Yang, P. *Science* **2001**, *292*, 1897–1899.
- (6) Kolmakov, A.; Zhang, Y.; Cheng, G.; Moskovits, M. *Adv. Mater.* **2003**, *15*, 997–1000.
- (7) Liu, Q. C.; Xu, J. J.; Xu, D.; Zhang, X. B. *Nat. Commun.* **2015**, *6*, 7892.
- (8) Ju, S.; Facchetti, A.; Xuan, Y.; Liu, J.; Ishikawa, F.; Ye, P.; Zhou, C.; Marks, T. J.; Janes, D. B. *Nat. Nanotechnol.* **2007**, *2*, 378–384.
- (9) Chen, X.; Tong, Y.; Wang, G.; Tang, Q.; Liu, Y. *Appl. Phys. Lett.* **2015**, *107*, 233503.
- (10) Goldberger, J.; Sirbuly, D. J.; Law, M.; Yang, P. *J. Phys. Chem. B* **2005**, *109*, 9–14.

- (11) Chatman, S.; Emberley, L.; Poduska, K. M. *ACS Appl. Mater. Interfaces* **2009**, *1*, 2348–2352.
- (12) Janotti, A.; Van de Walle, C. G. *Rep. Prog. Phys.* **2009**, *72*, 126501.
- (13) Wang, C.; Du, G. H.; Stahl, K.; Huang, H. X.; Zhong, Y. J.; Jiang, J. Z. *J. Phys. Chem. C* **2012**, *116*, 4000–4011.
- (14) Orlov, A. M.; Kostishko, B. M.; Gonchar, L. I. *Tech. Phys. Lett.* **1998**, *24*, 81–82.
- (15) Neal, A. T.; Mou, S.; Lopez, R.; Li, J. V.; Thomson, D. B.; Chabak, K. D.; Jessen, G. H. *Sci. Rep.* **2017**, *7*, 13218.
- (16) Ueda, N.; Hosono, H.; Waseda, R.; Kawazoe, H. *Appl. Phys. Lett.* **1997**, *70*, 3561–3563.
- (17) Zhou, W.; Xia, C.; Sai, Q.; Zhang, H. *Appl. Phys. Lett.* **2017**, *111*, 242103.
- (18) King, P. D.; Veal, T. D. *J. Phys.: Condens. Matter* **2011**, *23*, 334214.
- (19) Yang, X.; Wolcott, A.; Wang, G.; Sobo, A.; Fitzmorris, R. C.; Qian, F.; Zhang, J. Z.; Li, Y. *Nano Lett.* **2009**, *9*, 2331–2336.
- (20) Philip, J.; Punnoose, A.; Kim, B. I.; Reddy, K. M.; Layne, S.; Holmes, J. O.; Satpati, B.; Leclair, P. R.; Santos, T. S.; Moodera, J. S. *Nat. Mater.* **2006**, *5*, 298–304.
- (21) Kohan, A. F.; Ceder, G.; Morgan, D.; Van de Walle, C. G. *Phys. Rev. B: Condens. Matter Mater. Phys.* **2000**, *61*, 15019–15027.
- (22) Singh, A. K.; Janotti, A.; Scheffler, M.; Van de Walle, C. G. *Phys. Rev. Lett.* **2008**, *101*, 055502.
- (23) Samson, S.; Fonstad, C. G. *J. Appl. Phys.* **1973**, *44*, 4618–4621.
- (24) Soleimani, V.; Ghasemi Varnamkhasi, M. *J. Electron. Mater.* **2016**, *45*, 5395–5403.
- (25) Liu, Z. Q.; Li, C. J.; Lü, W. M.; Huang, X. H.; Huang, Z.; Zeng, S. W.; Qiu, X. P.; Huang, L. S.; Annadi, A.; Chen, J. S.; Coey, J. M. D.; Venkatesan, T.; Ariando. *Phys. Rev. X* **2013**, *3*, 021010.
- (26) Dittrich, T.; Weidmann, J.; Koch, F.; Uhlendorf, I.; Lauermaun, I. *Appl. Phys. Lett.* **1999**, *75*, 3980–3982.
- (27) Bansal, S.; Pandya, D. K.; Kashyap, S. C.; Haranath, D. *J. Alloys Compd.* **2014**, *583*, 186–190.
- (28) Persson, A. I.; Larsson, M. W.; Stenstrom, S.; Ohlsson, B. J.; Samuelson, L.; Wallenberg, L. R. *Nat. Mater.* **2004**, *3*, 677–681.
- (29) Hochbaum, A. I.; Fan, R.; He, R. R.; Yang, P. D. *Nano Lett.* **2005**, *5*, 457–460.
- (30) Hwang, Y. J.; Boukai, A.; Yang, P. D. *Nano Lett.* **2009**, *9*, 410–415.
- (31) Suzuki, M.; Hidaka, Y.; Yanagida, T.; Klamchuen, A.; Kanai, M.; Kawai, T.; Kai, S. *Phys. Rev. E* **2011**, *83*, 061606.
- (32) Klamchuen, A.; Yanagida, T.; Kanai, M.; Nagashima, K.; Oka, K.; Kawai, T.; Suzuki, M.; Hidaka, Y.; Kai, S. *Appl. Phys. Lett.* **2010**, *97*, 073114.
- (33) Anzai, H.; Suzuki, M.; Nagashima, K.; Kanai, M.; Zhu, Z.; He, Y.; Boudot, M.; Zhang, G.; Takahashi, T.; Kanemoto, K.; Seki, T.; Shibata, N.; Yanagida, T. *Nano Lett.* **2017**, *17*, 4698–4705.
- (34) Bjork, M. T.; Schmid, H.; Knoch, J.; Riel, H.; Riess, W. *Nat. Nanotechnol.* **2009**, *4*, 103–107.
- (35) Perea, D. E.; Hemesath, E. R.; Schwalbach, E. J.; Lensch-Falk, J. L.; Voorhees, P. W.; Lauhon, L. *Nat. Nanotechnol.* **2009**, *4*, 315–319.
- (36) Moreno, M. S.; Egerton, R. F.; Midgley, P. A. *Phys. Rev. B: Condens. Matter Mater. Phys.* **2004**, *69*, 233304.
- (37) Meng, G.; Zhuge, F. W.; Nagashima, K.; Nakao, A.; Kanai, M.; He, Y.; Boudot, M.; Takahashi, T.; Uchida, K.; Yanagida, T. *ACS Sensors* **2016**, *1*, 997–1002.